Validation of Just-Released SWOT L2 KaRIn Beta Prevalidated Data Based on Restore the Marine Gravity Field and Its Application

Hengyang Guo, Xiaoyun Wan, and Huaibing Wang

Abstract—**A part of the preprocessed beta Ka-band radar interferometer (KaRIn) data (7 September–21 November 2023) for the surface water and ocean topography (SWOT) mission has been released. To validate the performance of SWOT L2 KaRIn beta prevalidated data (beta data), this study conducted various experiments, including inverting the ocean gravity field and seafloor topography from these data, validating the accuracy of the deflections of the vertical (DOV) by DOV products of Scripps Institution of Oceanography (SIO). The root mean square of differences between north–south and east–west components is about 1.83 urad and 2.71 urad, respectively. The precision of gravity anomaly (SWOT_GA) is about 5.07 mGal compared with shipborne gravity. The results derived from one-cycle data are comparable with those obtained from a substantial dataset accumulated by traditional nadir altimeters. The accuracy of seafloor topography inverted from SWOT_GA is about 68 m validated by shipborne depth, which is almost the same as the topography obtained from SIO_GA and SDUST2021GRA. The results of multiple experiments have demonstrated that beta data can be used to compute high-precision ocean gravity fields and seafloor topography products. This proves the success of the first operational run of KaRIn and the capability of SWOT to support studies related to ocean science. The current evaluation results are based on beta data. The prevalidated data will be more accurate after further calibration, which will lead to higher accuracy of the inverted gravitational field products in the future.**

Index Terms—**Gravity anomalies (GA) and bathymetry, performance of SWOT L2 Ka-band radar interferometer (KaRIn) beta prevalidated data, radar interferometry, surface water and ocean topography (SWOT) mission.**

I. Introduction

The surface water and ocean topography (SWOT) satellite, jointly developed by the National Aeronautics and Space Administration and Centre National d'Études Spatiales (CNES), was successfully launched in December 2022. The development, launch, and operation of the SWOT satellite have attracted international attention across various fields [1], [2]. The Ka-band radar interferometer (KaRIn) carried by SWOT can provide 2-D sea surface height (SSH) data, enabling the acquisition of a higher spatial resolution (< 2 km) ocean gravity field, which cannot be achieved by traditional nadir altimeters. Currently, the L2 KaRIn beta prevalidated data (beta data) are released by the SWOT team (7 September–21 November 2023) (Note that the quality of the beta prevalidated product is not final and will be affected by some evolutions, as some deficiencies were well-identified by the SWOT project) [3]. All beta data are being reprocessed by optimal algorithms and calibration to generate prevalidated science data, which is planned for release soon. Despite the incompleteness of the beta data, the conditions for inversion of the ocean gravity field based on one cycle are already in place.

Before the real measured data are published, many scholars have done a lot of research based on the simulated data, which provides experiences for inverting the ocean gravity field. Jin et al. [4] simulated various errors associated with the SWOT satellite using power spectral density (PSD) data provided by Esteban-Fernandez et al. [5] in the budget of SWOT errors. In the South China Sea and part of the Indian Ocean, significant improvements are observed in the accuracy of the east–west component of the deflections of the vertical (DOV). The authors in [4] and [6] have analyzed the instrumental errors of interferometric radar altimeters and their impact on DOV. Wan et al. [7] investigated the influence of environmental errors on the recovery of DOV and gravity anomalies (GA) based on wide-swath observations. Yu et al. [8] simulated the observations of SWOT and recovered the GA using the inverse Vening-Meinesz (IVM) formula and the inverse Stokes integral method (ISM). Experiments demonstrated that the IVM exhibits more robustness in handling both random and systematic errors within the SWOT dataset compared with ISM. Ma et al. [9] performed cross calibration within one cycle using simulated data and then conducted a collinear adjustment over multiple cycles. Compared with one cycle, this strategy improved the accuracy of GA by approximately 45%.

As estimated by Sandwell et al. [10] in 2006, creating a global unified bathymetric map using only multibeam measurements requires hundreds of years and billions of dollars. According to statistics from the National Oceanography Center in the United Kingdom, approximately 24.9% of the above jobs have been completed as of 2023. It is estimated that, if relying solely

Manuscript received 28 December 2023; revised 9 March 2024; accepted 23 March 2024. Date of publication 29 March 2024; date of current version 12 April 2024. This work was supported in part by the National Natural Science Foundation of China under Grant 42074017 and in part by the Key Laboratory of Smart Earth under Grant KF2023YB01-12. *(Corresponding author: Xiaoyun Wan.)*

The authors are with the School of Land Science and Technology, China University of Geosciences, Beijing 100089, China (e-mail: ghy2022@email.cugb.edu.cn; wanxy@cugb.edu.cn; 2012210016@email.cugb.edu.cn).

Digital Object Identifier 10.1109/JSTARS.2024.3382976

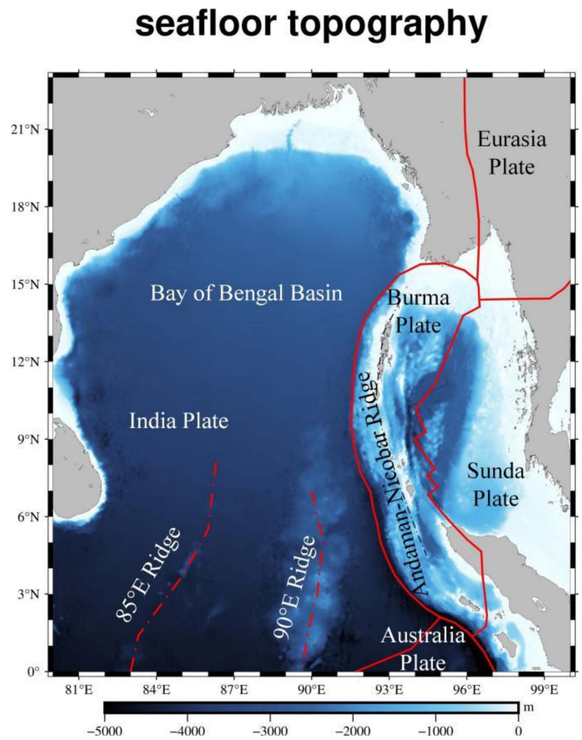

Fig. 1. Bay of Bengal and its surrounding areas.

on shipborne data, completing this project would still require another 120 years. Satellite altimetry has become the most crucial technology for inverting ocean gravity fields and seafloor topography due to its advantages, such as shorter data acquisition cycles and wider measuring ranges [11], [12]. Based on the altimetry data, the high-precision and high-resolution models of DOV and GA are inverted [4], [13], [14].

The gravity field products provided by satellite altimetry constitute an important data source for inverting seafloor topography, particularly the GA data [15]. Liu et al. [16] conducted seafloor topography models for the Emperor Seamount chain by combining shipborne depth data with GA models. They found that higher resolution GA models resulted in higher inversion accuracy. Annan and Wan [17] utilized an improved gravity geology method, combining airborne air-free GA and shipborne depth data, to construct a depth model for the Gulf of Guinea. Wan et al. [18] used the GA data restored from the HY-2A/GM data to compute the bathymetry model over the Gulf of Guinea. Their results indirectly demonstrate that the altimetry data provided by HY-2A can be used for ocean gravity field inversion. Annan and Wan [15] employed convolutional neural networks to predict seafloor topography models for the Guinea Basin region using ocean gravity field data.

This study aims to assess beta data by inverting the gravity field and seafloor topography of the Bay of Bengal and its surrounding areas (abbreviated as BOB). The rest of the article is organized as follows. In Section II, the research area and data are introduced. Section III presents the method to compute DOV and GA in the study areas (short-named SWOT_DOV and SWOT_GA). The method for deriving seafloor bathymetry from SWOT_GA is also described (named SWOT_BAT). In Section IV, the precision of SWOT_DOV and SWOT_GA is validated by multiple datasets. The accuracy of the SWOT_BAT derived from SWOT_GA is evaluated by shipborne depth data. The results assess the application of SWOT beta data in ocean science research. Section V discusses the precision of gravity field and seafloor topography recovered by multiple-cycle data. The results of residual DOV are analyzed. Finally, Section VI concludes this article.

II. Study Areas and Data

A. Study Areas

The study area is focused on the BOB (80°E–100°E, 0°N–23°N). This region encompasses the largest delta system and basin in the world, resulting in intricate seafloor topography [19], [20]. The location of the study area and its seafloor topography are plotted in Fig. 1.

B. Data

The datasets adopted in this study are listed in Table I.

The beta data used in the experiment are provided by AVISO, with a cycle of 21 days, and the interval of the grid is about 2 km. The ground track of one-cycle beta data is shown in Fig. 2.

SSH data are calculated from SWOT beta data (variable named "ssha_karin") and mean sea surface (MSS) data [21]. In addition, it is necessary to interpolate mean dynamic topography (MDT) data [22] to the corresponding grid points of SSH. This process involves subtracting the seafloor topography to obtain the geoid height.

In the process of obtaining DOV and GA, it is essential to employ a remove-and-restore method to mitigate the impact of long-wavelength errors. The residual geoid height in the experiment is derived by removing the geoid gradient calculated from the XGM2019e model, a highly accurate global gravity field model [23]. The final DOV and GA are then obtained by adding the background field provided by the XGM2019e model. To validate the accuracy of the results, we utilize DOV (east_32.1 and north_32.1) and GA (grav_32.1) models provided by the Scripps Institution of Oceanography (SIO) [24], shipborne gravity data provided by the National Centers for Environmental Information (NCEI), as well as the SDUST2021GRA provided by the Shandong University of Science and Technology (SDUST).

The seafloor topography models used include DTU21 provided by the Technical University of Denmark (DTU), Topo_25.1 provided by SIO, and ETOPO1 provided by National Oceanic and Atmospheric Administration (NOAA). All of them are internationally recognized for their high precision [25]. The seafloor topography of the research area, as illustrated in Fig. 1, is based on the DTU21.

Shipborne gravity data constitute a compiled set of measured ocean gravity data collected by various departments using different instruments [26]. Before using the shipborne gravity data, it needs to be adjusted by removing gross errors using a quadratic polynomial in time [27]. Shipborne depth data also

TABLE I
INFORMATION OF THE DATASETS USED IN THIS ARTICLE

Datasets	Provider
SWOT Beta data	AVISO
MSS MSS_CNES_CLS2015 (1')	CNES
MDT MDT_CNES_CLS18 (7.5')	CNES
DTU21 bathymetric model (1')	DTU
ETOPO1 (1')	NOAA
SDUST2021GRA (1')	SDUST
XGM2019e (1')	Technical University of Munich
SIO V32.1 datasets (1')	SIO
Shipborne gravity data and depth data	NCEI

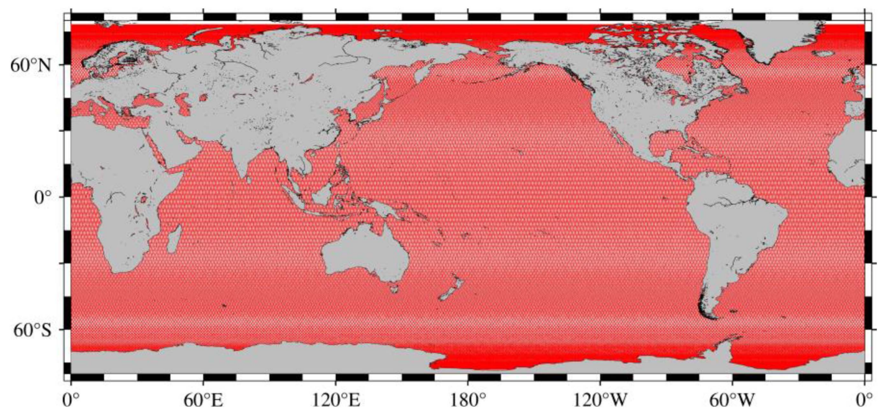

Fig. 2. Ground track of one-cycle beta data.

require preprocessing. It is necessary to remove the gross errors based on the ETOPO1 model [28].

III. Methodology

A. Restore DOV and GA From SWOT Wide-Swath Data

The interval of beta data is less than 2 km, and a total of 68 columns of data are composed in one pass file. Based on the data processing experience from the work of [4] and [8], the wide-swath data can be split into along-track and across-track directions. By utilizing information from adjacent points in multiple directions, the geoid gradients will be calculated, as shown in Fig. 3.

In Fig. 3, the blue dots (the shape of the blue circle and the blue square just to distinguish between the adjacent two columns of SSH grid data) represent SSH grid data. The red dots represent the geoid gradient calculated from the blue dots. Before calculating the residual geoid gradient, the data need to be preprocessed. The wide-swath data are split into eight directions according to the direction of along track, cross track, and two oblique tracks. These directions are shown by green dotted lines in Fig. 3. The split data in each direction are stored in 1-D columns to calculate the residual geoid gradient. It should be noted that if the data are on the edge of the swath, then there are no data on the left or right side; the data can only be split in

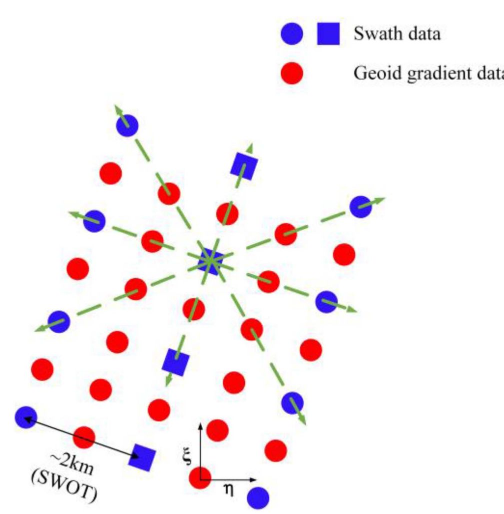

Fig. 3. Split beta data into along-track and across-track directions.

five directions. After the data preprocessing, the geoid gradient can be computed based on the geoid heights between adjacent two points

$$e = \frac{\partial N}{\partial \psi} \tag{1}$$

where e is the geoid gradient, and ψ is the spherical distance between the two points.

The residual DOV is calculated by the LSC method [29], [30]. The LSC combines the calculation of DOV and the grid transformation of DOV into one step

$$\begin{pmatrix} \xi_{\text{res}} \\ \eta_{\text{res}} \end{pmatrix} = \begin{pmatrix} C_{\xi e} \\ C_{\eta e} \end{pmatrix} (C_{ee} + C_n)^{-1} e \quad (2)$$

where ξ_{res} and η_{res} are the north component and the east component of residual DOV, respectively. $C_{\xi e}$ is the covariance matrix between the north component of DOV and the residual geoid gradient, and $C_{\eta e}$ is the covariance matrix between the prime vertical component of DOV and the residual geoid gradient. C_{ee} is the variance matrix for the gradient. C_n is a diagonal matrix containing the noise variances of the geoid gradient. e is calculated by (1).

Using the IVM formula, select the appropriate kernel function and solve for the GA based on the grid DOV [30], [31]. The 1-D fast Fourier transform (FFT) method and IVM formula are used to derive the GA from the DOV [30]. Since the difference in latitude is taken into account in the calculation of spherical latitude by the 1-D FFT method, the algorithm is more rigorous in theory [12]

$$\Delta g\,(p) = \frac{\gamma_0}{4\pi} \iint_\sigma H'\,(\psi)\,(\xi_q \cos\alpha_{qp} + \eta_q \sin\alpha_{qp})\, d\sigma_q \quad (3)$$

where $\Delta g(p)$ is the GA at point p. $\gamma_0 = \frac{GM}{R^2}$, GM is the gravitational constant, and R is the mean Earth radius. α_{qp} is the azimuth from point q to point p. ξ_q and η_q are the meridian component and the prime vertical component of the DOV at point q, respectively. $H'(\psi)$ is the derivative of the kernel function, $H(\psi) = \frac{1}{\sin\frac{\psi}{2}} + \log\left(\frac{\sin^3\frac{\psi}{2}}{1+\sin\frac{\psi}{2}}\right)$, where ψ is the spherical distance between point q and point p.

The ψ cannot be zero in the derivative of the kernel function. We must consider the influence of the inner zone effect on GA derivation [29], [32]

$$\Delta g = \frac{s_0\gamma_0}{2}\,(\xi_x + \eta_y) \quad (4)$$

where ξ_x and η_y are the change rates of the meridian and prime vertical component of DOV, respectively. s_0 is the size of the inner zone. Δx and Δy are the distances of the grid, respectively. Finally, DOV and GA are restored using the XGM2019e.

B. Bathymetry Inversion From GA

In the frequency-domain equation, the depth consists of two parts, one is long-wavelength depth and another is passband depth. The predicted depth can be obtained as follows [25], [33]:

$$h_{\text{predict}} = h_{\text{long}} + h_{\text{passband}} \quad (5)$$

where h_{predict} is the inverted depth, h_{long} is the long-wavelength depth, and h_{passband} is the passband depth

$$h_{\text{passband}} = F^{-1}\left[\frac{1}{2\pi G\Delta\rho} e^{kd} F(\Delta g)\right] \quad (6)$$

where F denotes the FFT method [34]. G is the gravitational constant, and $\Delta\rho$ denotes the density contrast between the upper crust and seawater. e^{kd} is a continuation method, d is the datum depth, and k is the wavenumber. $k = (k_x, k_y)$, where $k_x = \frac{2\pi}{\lambda_x}$ and $k_y = \frac{2\pi}{\lambda_y}$; λ_x and λ_y represent the wavelengths in the x- and y-direction, respectively. $F(\Delta g)$ is the FFT value of GA, $F(\Delta g) = 2\pi G\Delta\rho e^{-kd} \sum_{n=1}^{\infty} (\frac{k^{n-1}}{n!} \cdot F(h^n))$. If only considering the linearity term, i.e., $n = 1$, we can get (6). The shipborne depth data at control points are often used to calculate long-wavelength depth [35], [36].

GA can be used to invert the seafloor topography in medium and short wavelength bands [37], [38], [39], [40]. The mentioned passband depth is the depth calculated based on GA after processing by the passband filter. The passband filter is a combination of a high-pass filter and a low-pass filter [37]

$$w = w_1(k) \cdot w_2(k) \quad (7)$$

where $w_1(k)$ is the high-pass filter, $w_1(k) = 1 - e^{-\frac{1}{2}(ks)^2}$, and $s = \frac{\sqrt{2\ln 2}}{k}$. And $w_2(k)$ is the low-pass filter, $w_2(k) = \left(1 + \text{A}\left(\frac{k}{2\pi}\right)^4 e^{2kd}\right)^{-1}$, and $A = \lambda^4 e^{-\frac{4\pi d}{\lambda}}$.

The cutoff wavelength is usually derived by correlation analysis between GA and submarine topography [25], [41], [42]. Based on the analysis, this article uses 20–120 km as the cutoff wavelength in the passband filter.

TABLE II
STATISTICS OF SWOT BETA DATA

Dataset	Data	Number of Passes	Number of missing
Cycle 3	Pass 170–584	434	10
Cycle 4	Pass 160–584	405	19
Cycle 5	Pass 001–584	549	35
Cycle 6	Pass 001–544	521	23

IV. Results and Analysis

The beta data available now include four cycles. Some pass files are missing within each cycle. Cycle 6 is only updated until Pass 544. The number of data is summarized in Table II.

In this section, SWOT_DOV and SWOT_GA are computed based on Cycle 5 (the largest amount of one-cycle beta data).

A. Results of DOV

The LSC method is utilized to calculate residual DOV in the study areas. The SWOT_DOV is restored through the XGM2019e model, and the grid resolution is $1' \times 1'$. The results are depicted in Fig. 4. Comparing the SWOT_DOV with the SIO_DOV, the results are presented in Fig. 5 and Table III.

Compared with SIO_DOV, the root mean square (RMS) of differences in the east–west direction is 2.72 urad. The RMS of differences in the north–south direction is 1.83 urad. The results indicate that the KaRIn aboard SWOT is capable of measuring the SSH with high accuracy. In contrast to the results calculated by Ji et al. [19] using HY-2A/GM data, SWOT_DOV achieves a similar accuracy using only one-cycle data, surpassing the results derived from three-year accumulation. As the inclination

TABLE III
STATISTICS OF THE COMPARISON BETWEEN SWOT_DOV AND SIO_DOV (UNIT: URAD)

component	Min	Max	Mean	STD	RMS
North	–44.17	36.27	–0.01	1.83	1.83
East	–49.29	52.66	0.16	2.71	2.72

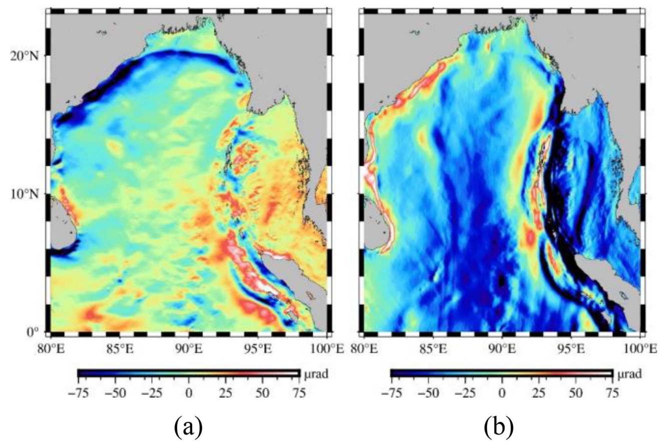

Fig. 4. DOV of BOB. (a) Component ζ. (b) Component η.

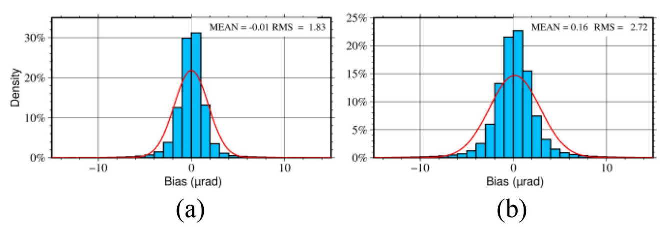

Fig. 5. Histogram of precision of SWOT_DOV validated by SIO_DOV. (a) Component ζ. (b) Component η.

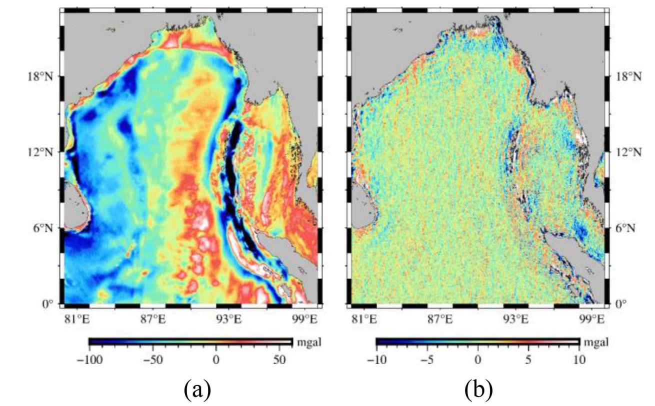

Fig. 6. SWOT_GA. (a) SWOT_GA. (b) Validation of SWOT_GA by SIO_GA.

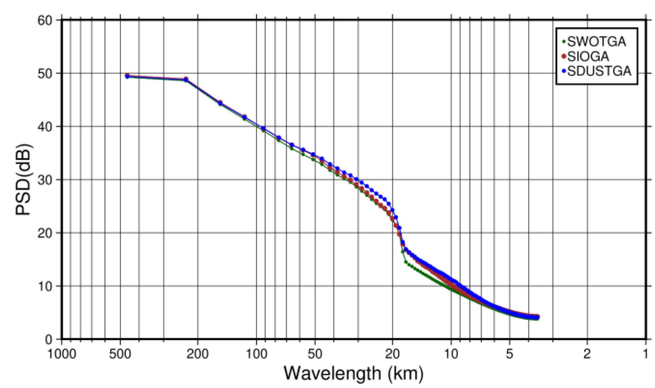

Fig. 7. PSD of three GA models.

of SWOT is 77.6°, as analyzed by Ma et al. [9], there is an improvement in the accuracy of the east–west component of DOV. But it still lags behind the accuracy of the north–south component. Overall, the precision of SWOT_DOV in this experiment has improved, although the east–west component remains less accurate than the north–south component.

B. Results of GA

The GA for the BOB based on SWOT with a grid resolution of $1' \times 1'$ has been computed using IVM, as shown in Fig. 6.

Juxtaposing Fig. 6 with the seafloor topography (as shown in Fig. 1), it can be seen that the obvious differences between SWOT_GA and SIO_GA concentrate in the junction of the Indian Plate and Burma Plate, and Burma Plate and Sunda Plate, where the values of the SWOT_DOV, as shown in Fig. 4, are also relatively high. In addition, large differences are also found in the northern part of the Bay of Bengal Basin and the eastern and northern parts of the Sunda plate, which are bordered by land. The nearshore may be disturbed by more factors, such as complex and variable seafloor topography and wave variations.

Plotting the PSD of SWOT_GA, SIO_GA, and SDUST2021GRA, as shown in Fig. 7, for wavelength less than 20 km, SWOT_GA exhibits the smallest values, while SDUST2021GRA has the largest values. This suggests that SDUST2021GRA has a richer high-frequency signal. The main reason is that it incorporates multiple altimetry data. On the other hand, SWOT_GA has less high-frequency signal, as it relies solely on one-cycle beta data. When the wavelength is greater than 100 km, there is no significant difference in the signals among the three models.

The SWOT_GA is compared with the SIO_GA, SDUST2021GRA, and the shipborne gravity data, respectively. The results are presented in Table IV.

The RMS of differences between SWOT_GA and SIO_GA is 3.29 mGal. The RMS of differences between SWOT_GA and SDUST2021GRA is 2.13 mGal. The differences between SWOT_GA and shipborne gravity in the entire research area are larger, with an RMS of 5.07 mGal. The SWOT_GA for this research area inversion from wide-swath data is closer

TABLE IV
STATISTICS OF THE VALIDATION OF SWOT_GA (UNIT: MGAL)

Derived model	Min	Max	Mean	STD	RMS
SIO_GA-SWOT_GA	–86.73	55.98	0.31	3.28	3.29
SDUST2021GRA-SWOT_GA	–32.58	24.11	1.34E-3	2.13	2.13
NCEI-SWOT_GA	–29.97	29.99	0.10	5.07	5.07

TABLE V
VALIDATION OF SWOT_GA AT DIFFERENT DISTANCES FROM THE COASTLINE

distance from coastline (km)	Min (mGal)	Max (mGal)	Mean (mGal)	STD (mGal)	RMS (mGal)
>10	–86.73	35.29	0.21	2.73	2.74
>20	–29.49	26.95	0.21	2.48	2.48
>30	–26.83	24.39	0.21	2.32	2.33
>40	–19.73	24.13	0.21	2.20	2.21
>50	–19.73	20.48	0.19	2.10	2.11

to SDUST2021GRA. Compared with the GA for the same research area by Ji et al. [20] inverted from CryoSat-2 altimetry data, the accuracy of one-cycle results is comparable with the accuracy obtained from six-month data by the CryoSat-2. This demonstrates the successful application of the KaRIn carried out by the SWOT. The beta data from SWOT can be used to invert high-precision marine gravity field products. Analyze the differences between SWOT_GA and SIO_GA according to the distance from the coastline. The detailed results are shown in Table V.

In Table V, as the distance to the coastline increases, the differences between SWOT_GA and SIO_GA gradually diminish. Particularly, when excluding grid points within 10 km of the shore, the RMS of differences between the two models reduces to 2.74 mGal. When assessing more than 50 km offshore, the RMS of differences is less than 2.11 mGal. This affirms that the accuracy of the nearshore SSH is not as high as data away from the coast. The low quality of the nearshore altimetry data leads to the low accuracy of the GA in the nearshore.

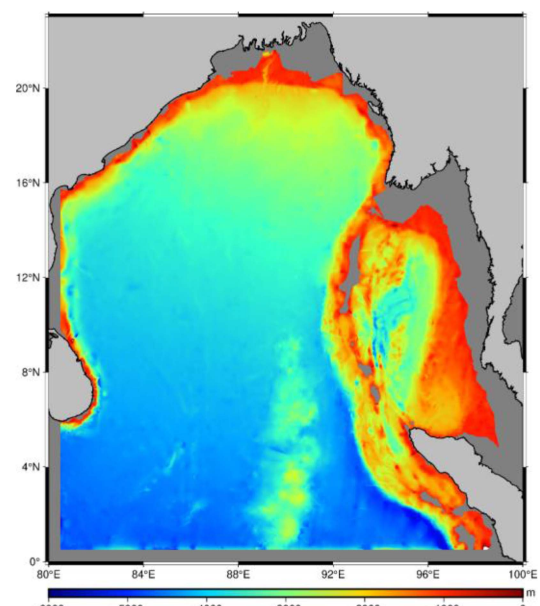

Fig. 8. Depth derived by SWOT_GA.

C. Performance in Inverting the Seafloor Topography

We employed a frequency-domain method to invert the SWOT_BAT based on SWOT_GA, and the results are depicted in Fig. 8. The SWOT_BAT is calculated based on the SWOT_GA, as recovered in Section IV-B, to indirectly prove the performance of the beta data of SWOT. To eliminate boundary effects, the range of the study area is contracted during the water depth inversion. In this experiment, the contracted scope of the study area is (81°E–99°E, 1°N–22° N), resulting in missing data in Fig. 8. The substantial data gaps in the northern and eastern parts of the study area are due to the absence of shipborne depth data in those regions.

We additionally calculate two bathymetry models from SIO_GA and SDUST2021GRA (named SIO_BAT and SDUST_BAT). Compare the three models with shipborne depth data. Gross errors are removed based on three standard deviation (STD) criteria. The results are presented in Table VI. The statistics are conducted for depths exceeding 100 m [25], [36].

The STD of differences between the three topography models and shipborne depth is 67.88 m, 65.81 m, and 65.82 m, respectively. The removal rates of gross errors for SIO_BAT and SDUST_BAT are 2.23% and 2.29%, respectively. With similar removal rates of gross errors, the accuracy of SIO_BAT is slightly higher than SDUST_BAT. The accuracy of SWOT_BAT demonstrates slightly lower accuracy than the other two models, the removal rate of gross errors is 2.23%. The PSD of the three topography models is shown in Fig. 9. The PSD curves appear to be approximately consistent. The signal energy of SWOT_BAT is comparable to that of SIO_BAT and SDUST_BAT. This indirectly confirms the reliability of the beta data, which can

TABLE VI
PRECISION STATISTICS OF BATHYMETRY MODELS AFTER REMOVING GROSS ERRORS

Bathymetry	Min (m)	Max (m)	Mean (m)	STD (m)	Removal Ratio
SWOT_BAT	–313.66	338.08	11.57	67.88	2.23%
SIO_BAT	–313.32	342.25	12.39	65.81	2.23%
SDUST_BAT	–314.99	346.29	12.11	65.82	2.29%

TABLE VII
VALIDATIONS OF BATHYMETRY MODELS AT DIFFERENT DISTANCES FROM THE COASTLINE

distance from coastline (km)	Bathymetry	Min (m)	Max (m)	Mean (m)	STD (m)
>10	SWOT_BAT	–292.05	320.66	11.30	60.08
	SIO_BAT	–288.33	318.09	11.99	59.98
	SDUST_BAT	–290.04	319.29	11.44	59.15
>30	SWOT_BAT	–276.68	306.74	11.51	57.49
	SIO_BAT	–272.16	304.23	12.22	57.76
	SDUST_BAT	–274.54	305.86	11.82	57.00
>100	SWOT_BAT	–228.08	257.18	10.50	49.43
	SIO_BAT	–225.80	256.66	10.94	49.60
	SDUST_BAT	–227.75	258.59	10.94	48.95

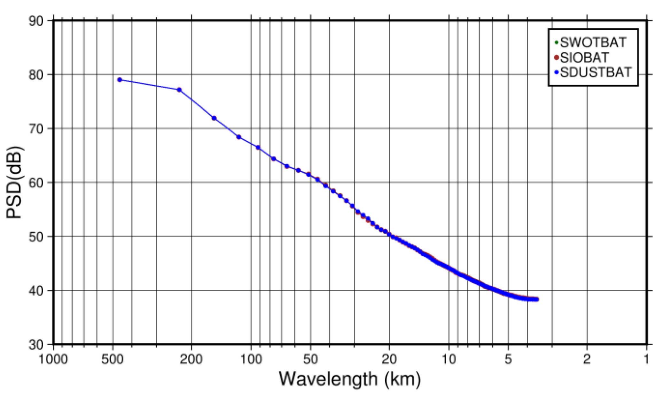

Fig. 9. PSD of three bathymetry models.

meet the requirements for inverting marine GA and seafloor topography.

Those results confirm that, in the research areas, the accuracy of SWOT_GA is comparable with SIO_GA and SDUST2021GRA. The outcome indirectly validates the high-precision measurement capability of KaRIn carried out by SWOT. This capability can provide high-precision wide-swath data for ocean gravity field inversion. Three models and the results of validation are illustrated in Fig. 10.

From Fig. 10(a) to (c), there are minimal differences in values between SWOT_BAT and the other two models. However, upon analyzing the details of the models, some noticeable differences emerge. For instance, in the region of (11°N–12°N, 83°E–84°E), the values of SWOT_BAT are significantly larger, making these details more pronounced. The data for each model at different distances from the shore are compared with the shipborne depth, and the results are shown in Table VII.

Table VII reveals a noticeable improvement in the accuracy of the bathymetry models as the distance from the coastline increases. The accuracy of the SWOT_BAT is consistent with the other two topography models. Focus on the relationship between the accuracy of SWOT_BAT and the distance from the coastline, it becomes evident that the accuracy of measuring SSH nearshore is low. This implies that the KaRIn altimeter is influenced by coastal areas. The conclusion is similar to the analysis presented in Table V.

V. DISCUSSION

In Section IV, the experiments utilized Cycle 5 (the largest amount of data) to compute SWOT_DOV, SWOT_GA, and SWOT_BAT. The results demonstrated that the accuracy of results is at a commendable level. Cycle 4 has the smallest amount of data, and the validation of SWOT_DOV and SWOT_GA computed using Cycle 4 is presented in Table VIII.

By comparing the results of Cycle 4 and those of Cycle 5, it can be seen that the absence of 144-pass files does not significantly impact the outcomes. Apart from the fact that the missing data are not concentrated in the study area, another crucial factor is the advantage of the new wide-swath mode. The novel KaRIn brings massive data for the experiments. Even Cycle 4, which has the fewest pass files, provides more than 1.8

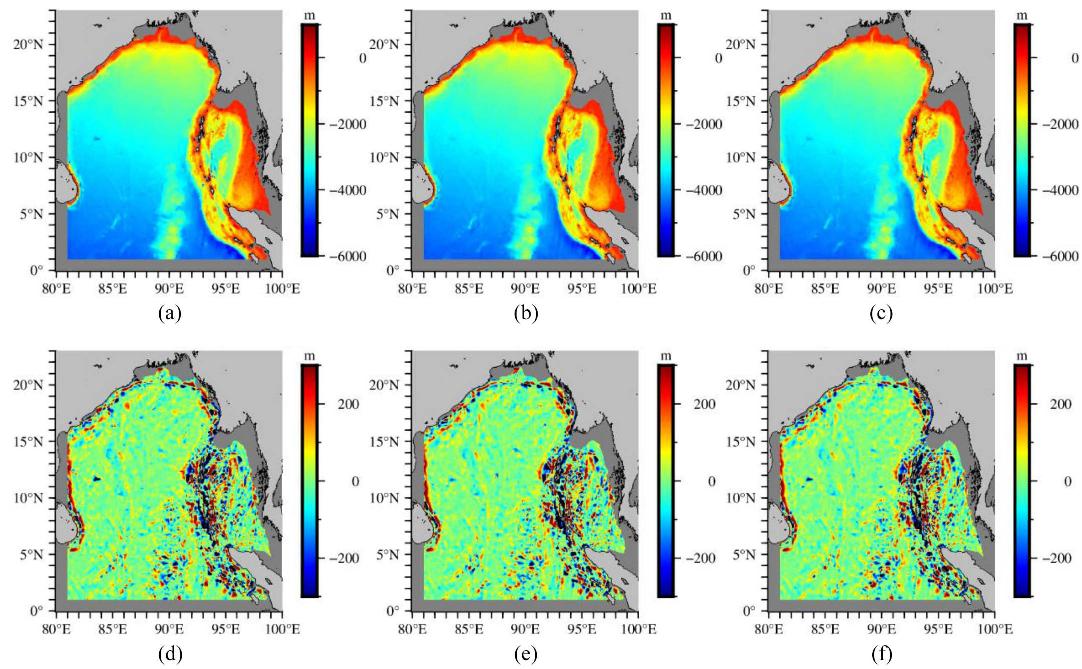

Fig. 10. Bathymetry and its error distribution. (a) SWOT_BAT. (b) SIO_BAT. (c) SDUST_BAT. (d) Error distribution of SWOT_BAT. (e) Error distribution of SIO_BAT. (f) Error distribution of SDUST_BAT.

TABLE VIII
ACCURACY STATISTICS FOR SWOT_DOV AND SWOT_GA CALCULATED BY CYCLE 4

component	Min	Max	Mean	STD	RMS
DOV-North (urad)	–44.17	36.28	–0.01	1.82	1.82
DOV-East (urad)	–49.28	52.67	0.15	2.71	2.71
SIO_GA-SWOT_GA (mGal)	–86.72	55.93	0.31	3.28	3.29
NCEI-SWOT_GA (mGal)	–29.90	30.15	0.11	5.06	5.06

TABLE IX
STATISTICS OF THE RESIDUAL SWOT_DOV (UNIT: URAD)

component	Min	Max	Mean	STD	RMS
North	–2.86	2.14	–0.03	0.26	0.26
East	–2.91	3.11	0.04	0.31	0.32

million available observations for the study area. The number of SSH data provided by Cycle 4 is sufficient to meet the calculation requirements for a $1'$ grid resolution in BOB.

However, the experiment has demonstrated that SWOT one-cycle data can invert high-precision gravity fields. It is important to note that the accuracy of the north–south component of DOV remains higher than the east–west component. To mitigate background field interference, directly analyze the residual SWOT_DOV computed by Cycle 4. The results are listed in Table IX.

From Table IX, the STD of the north–south component of residual DOV is only 0.05 urad higher than the east–west component. This proves that SWOT can significantly address the issue of inconsistent precision between the north–south and east–west components of DOV caused by the inclination of traditional altimetry satellites.

Using the mean value of four-cycle beta data, DOV, GA, and bathymetry are inverted. The accuracy of DOV is validated by SIO_DOV. The accuracy of GA and bathymetry is validated by shipborne gravity and shipborne depth data. In particular, the accuracy of topography focuses on data beyond 100 km from the coast, as listed in Table X.

From Table X, the accuracy of DOV, GA, and seafloor topography inverted from the averaged data is better than those obtained from one cycle. The results indicate that, after averaging, some biases can be eliminated in beta data. However, compared with the results calculated by one-cycle beta data, the current results show only light improvement in accuracy. We speculate that certain KaRIn instrument errors are not isolated but rather coupled with the SSH signals, such as roll error may still contribute to the bias. And the data are insufficiently available. In addition, the SWOT team is reprocessing KaRIn data with the best available algorithms and calibrations to generate prevalidated science data. Before the release of prevalidated data, beta data can meet the preprocessing needs of various oceanographic studies.

TABLE X
ACCURACY OF THE SWOT_GA AND THE SWOT_BAT CALCULATED BY FOUR-CYCLE DATA

component	Min	Max	Mean	STD
DOV-North (urad)	–34.11	36.27	0.01	1.75
DOV-East (urad)	–33.70	45.34	0.18	2.63
SWOT_GA (mGal)	–30.30	30.03	0.10	5.05
SWOT_BAT_100 km (m)	–223.06	261.70	10.94	49.36

VI. CONCLUSION

This study utilizes beta data to compute the gravity field and seafloor topography of the BOB. By assessing the accuracy of the inverted products, we evaluate the performance of the released beta data for ocean gravity field research. The residual SWOT_DOV data revealed consistent precision in both the north–south and east–west components, which proves that wide-swath data can greatly solve the problem of inconsistent component accuracy in both directions of DOV.

The accuracy of SWOT_DOV and SWOT_GA restored from one-cycle and four-cycle data demonstrates that the beta data of SWOT can be employed for high-precision gravity field recovery. Utilizing the frequency-domain method, we inverted the topography model based on SWOT_GA and confirmed its high accuracy by shipborne depth data. The results reflect the capability of SWOT to support studies related to ocean gravity and seafloor topography.

Despite the limited number of released beta data, our experiments have validated the remarkable potential of the KaRIn. The reprocessed data are expected to be released in the near future, which holds promise for more reliable wide-swath data. We need new methods to handle the abundance of 2-D SSH from wide-swath interferometric radar altimeters, enhancing data utilization and improving the precision of ocean gravity field inversion.

ACKNOWLEDGMENT

The authors would like to thank SIO for providing the SIO V32.1 model, DTU for providing the DTU21 bathymetric model, SDUST for providing the SDUST2021GRA, NOAA for providing the ETOPO1 model, TUM for providing the XGM2019e model, and CNES for providing MSS and MDT model for this study. The SWOT L2_LR_SSH data product is made freely available by the joint NASA/CNES SWOT project and the national programs that contribute to it. L2_LR_SSH product quality is not final and will be affected by some evolutions as the SWOT project team makes progress on science data processing algorithms and instrument calibrations.

REFERENCES

[1] L.-L. Fu and C. Ubelmann, "On the transition from profile altimeter to swath altimeter for observing global ocean surface topography," *J. Atmos. Ocean. Technol.*, vol. 31, no. 2, pp. 560–568, Feb. 2014, doi: 10.1175/JTECH-D-13-00109.1.

[2] L.-L. Fu, Y. Chao, L. Benoit, and L. Turki, "Mapping coastal sea level at high resolution with radar interferometry: The SWOT mission," presented at the AGU Fall Meeting, New Orleans, LA, USA, 2017.

[3] SWOT Project, "SWOT level-2 KaRIn low rate SSH basic (version PIB0)," 2023, Data accessed on: Nov. 2023, doi 10.24400/527896/A01-2023.013.

[4] T. Jin et al., "Analysis of vertical deflections determined from one cycle of simulated SWOT wide-swath altimeter data," *J. Geodesy*, vol. 96, no. 4, Apr. 2022, Art. no. 30, doi: 10.1007/s00190-022-01619-8.

[5] D. Esteban-Fernandez, L.-L. Fu, B. Pollard, P. Vaze, R. Abelson, and N. Steunou, "Swot project: Mission performance and error budget," Jet Propul. Lab., Pasadena, CA, USA, Tech. Rep. JPL D-79084, Apr. 2017.

[6] S. Tian, "Analysis of interferometric imaging radar altimeter errors on accuracy of marine gravity field inversion," M.S. thesis, Sch. Land Sci. Technol., China Univ. of Geosci., Beijing, China, 2019, doi: 10.27493/d.cnki.gzdzy.2019.001195.

[7] X. Wan, F. Wang, H. Guo, and B. Liu, "Impact of errors in environmental correction on gravity field recovery using interferometric radar altimeter observations," *Remote Sens.*, vol. 14, no. 24, Dec. 2022, Art. no. 6299, doi: 10.3390/rs14246299.

[8] D. Yu, C. Hwang, O. B. Andersen, E. T. Y. Chang, and L. Gaultier, "Gravity recovery from SWOT altimetry using geoid height and geoid gradient," *Remote Sens. Environ.*, vol. 265, Nov. 2021, Art. no. 112650, doi: 10.1016/j.rse.2021.112650.

[9] G. Ma, T. Jin, P. Jiang, J. Shi, and M. Zhou, "Calibration of the instrumental errors on marine gravity recovery from SWOT altimeter," *Mar. Geodesy*, vol. 46, no. 6, pp. 496–522, 2023, doi: 10.1080/01490419.2023.2232107.

[10] D. T. Sandwell et al., "Bathymetry from space: Rationale and requirements for a new, high-resolution altimetric mission," *Comptes Rendus Geosci.*, vol. 338, no. 14/15, pp. 1049–1062, Nov./Dec. 2006.

[11] B. Andersen, P. Knudsen, and P. A. M. Berry, "The DNSC08GRA global marine gravity field from double retracked satellite altimetry," *J. Geodesy*, vol. 84, no. 3, pp. 191–199, Mar. 2010, doi: 10.1007/s00190-009-0355-9.

[12] C. Zhu, X. Liu, J. Guo, S. Yu, and Y. Gao, "Sea surface heights and marine gravity determined from SARAL/AltiKa Ka-band altimeter over South China sea," *Pure Appl. Geophys.*, vol. 178, no. 1, pp. 1513–1527, Apr. 2021, doi: 10.1007/s00024-021-02709-y.

[13] L. Bao, H. Xu, and Z. Li, "Towards a 1 mGal accuracy and 1 min resolution altimetry gravity field," *J. Geodesy*, vol. 87, no. 10/12, pp. 961–969, Nov. 2013, doi: 10.1007/s00190-013-0660-1.

[14] D. T. Sandwell, R. D. Mueller, W. H. F. Smith, E. Garcia, and R. Francis, "New global marine gravity model from CryoSat-2 and Jason-1 reveals buried tectonic structure," *Science*, vol. 346, no. 6205, pp. 65–67, Oct. 2014, doi: 10.1126/science.1258213.

[15] R. F. Annan and X. Wan, "Recovering bathymetry of the Gulf of Guinea using altimetry-derived gravity field products combined via convolutional neural network," *Surv. Geophys.*, vol. 43, no. 5, pp. 1541–1561, Jul. 2022, doi: 10.1007/s10712-022-09720-5.

[16] P. Liu, S. Jin, and Z. Wu, "Assessment of the seafloor topography accuracy in the emperor seamount chain by ship-based water depth data and satellite-based gravity data," *Sensors*, vol. 22, no. 9, May 2022, Art. no. 3189, doi: 10.3390/s22093189.

[17] R. F. Annan and X. Wan, "Mapping seafloor topography of Gulf of Guinea using an adaptive meshed gravity-geologic method," *Arabian J. Geosci.*, vol. 13, no. 7, Mar. 2020, Art. no. 301, doi: 10.1007/s12517-020-05297-8.

[18] X. Wan, R. F. Annan, and W. Wang, "Assessment of HY-2A GM data by deriving the gravity field and bathymetry over the Gulf of Guinea," *Earth, Planets Space*, vol. 72, no. 1, Oct. 2020, Art. no. 151, doi: 10.1186/s40623-020-01291-2.

[19] H. Ji, J. Guo, C. Zhu, J. Yuan, X. Liu, and G. Li, "On deflections of vertical determined from HY-2A/GM altimetry data in the Bay of Bengal," *IEEE J. Sel. Topics Appl. Earth Observ. Remote Sens.*, vol. 14, pp. 12048–12060, 2021, doi: 10.1109/JSTARS.2021.3129273.

[20] H. Ji, X. Liu, C. Zhu, J. Yuan, B. Ji, and J. Guo, "On performance of CryoSat-2 altimeter data in deriving marine gravity over the Bay of Bengal," *Mar. Geophysical Res.*, vol. 42, no. 4, Dec. 2021, Art. no. 39, doi: 10.1007/s11001-021-09461-x.
[21] M. Pujol, P. Schaeffer, Y. Faugère, M. Raynal, G. Dibarboure, and N. Picot, "Gauging the improvement of recent mean sea surface models: A new approach for identifying and quantifying their errors," *J. Geophysical Res. Oceans*, vol. 123, no. 8, pp. 5889–5911, Aug. 2018, doi: 10.1029/2017JC013503.
[22] S. Mulet et al., "The new CNES-CLS18 global mean dynamic topography," *Ocean Sci.*, vol. 17, no. 3, pp. 789–808, Jun. 2021, doi: 10.5194/os-17-789-2021.
[23] P. Zingerle, R. Pail, T. Gruber, and X. Oikonomidou, "The combined global gravity field model XGM2019e," *J. Geodesy*, vol. 94, no. 7, Jul. 2020, Art. no. 66, doi: 10.1007/s00190-020-01398-0.
[24] D. T. Sandwell, H. Harper, B. Tozer, and W. H. F. Smith, "Gravity field recovery from geodetic altimeter missions," *Adv. Space Res.*, vol. 68, no. 2, pp. 1059–1072, Jul. 2021, doi: 10.1016/j. asr.2019.09.011.
[25] X. Wan, H. Wang, Y. Jia, and W. Ma, "Performance of Haiyang-2 derived gravity field products in bathymetry inversion," *Remote Sens.*, vol. 15, no. 1, Jan. 2023, Art. no. 32, doi: 10.3390/rs15010032.
[26] J. Guo, X. Liu, Y. Chen, J. Wang, and C. Li, "Local normal height connection across sea with ship-borne gravimetry and GNSS techniques," *Mar. Geophysical Res.*, vol. 35, no. 2, pp. 141–148, Jun. 2014, doi: 10.1007/s11001-014-9216-x.
[27] C. Hwang and B. Parsons, "Gravity anomalies derived from Seasat, Geosat, ERS-I and TOPEX/POSEIDON altimetry and ship gravity: A case study over the Reykjanes ridge," *Geophysical J. Int.*, vol. 122, no. 2, pp. 551–568, Sep. 1995, doi: 10.1111/j.1365-246x.1995.tb07013.x.
[28] C. Amante and B. Eakins, "ETOPO1 1 arc-minute global relief model: Procedures, data sources and analysis," NOAA Tech. Memorandum NESDIS NGDC-24, Washington, DC, USA, 2009. [Online]. Available: https://repository.library.noaa.gov/view/noaa/1163/noaa_1163_DS1.pdf
[29] R. H. Rapp, "Geos 3 data processing for the recovery of geoid undulations and gravity anomalies," *J. Geophysical Res. Atmos.*, vol. 84, no. B8, pp. 3784–3792, Aug. 1979, doi: 10.1029/JB084iB08p03784.
[30] C. Hwang, *High Precision Gravity Anomaly and Sea Surface Height Estimation From Geo-3/Seasat Altimeter Data*. Columbus, OH, USA: Ohio State Univ., 1989.
[31] W. Liang, J. Li, X. Xu, S. Zhang, and Y. Zhao, "A high-resolution earth's gravity field model SGG-UGM-2 from GOCE, GRACE, satellite altimetry, and EGM2008," *Engineering*, vol. 6, no. 8, pp. 860–878, Aug. 2020, doi: 10.1016/j.eng.2020.05.008.
[32] W. A. Heiskanen and H. Moritz, *Physical Geodesy*. San Francisco, CA, USA: Freeman, 1967.
[33] M. Hu, J. Li, H. Li, C. Shen, T. Jin, and L. Xing, "Predicting global seafloor topography using multi-source data," *Mar. Geodesy*, vol. 38, no. 2, pp. 176–189, Apr. 2015, doi: 10.1080/01490419.2014.934415.
[34] R. Parker, "The rapid calculation of potential anomalies," *Geophysical J. Int.*, vol. 31, no. 4, pp. 447–455, Mar. 1973, doi: 10.1111/j.1365-246X.1973.tb06513.x.
[35] X. Xiang, X. Wan, R. Zhang, Y. Li, X. Sui, and W. Wang, "Bathymetry inversion with the gravity-geologic method: A study of long-wavelength gravity modeling based on adaptive mesh," *Mar. Geodesy*, vol. 40, no. 5, pp. 329–340, Jul. 2017, doi: 10.1080/01490419.2017.1335257.
[36] D. An, J. Guo, Z. Li, B. Ji, X. Liu, and X. Chang, "Improved gravity-geologic method reliably removing the long-wavelength gravity effect of regional seafloor topography: A case of bathymetric prediction in the South China sea," *IEEE Trans. Geosci. Remote Sens.*, vol. 60, 2022, Art. no. 4211912, doi: 10.1109/TGRS.2022.3223047.
[37] W. H. F. Smith and D. T. Sandwell, "Bathymetric prediction from dense satellite altimetry and sparse shipboard bathymetry," *J. Geophysical Res.*, vol. 99, no. B11, pp. 21803–21824, Nov. 1994, doi: 10.1029/94JB00988.
[38] X. Wan, J. Ran, and S. Jin, "Sensitivity analysis of gravity anomalies and vertical gravity gradient data for bathymetry inversion," *Mar. Geophysical Res.*, vol. 40, no. 1, pp. 87–96, Mar. 2019, doi: 10.1007/s11001-018-9361-8.
[39] M. Hu, T. Jin, W. Jiang, Y. Chu, H. Wen, and J. Li, "Bathymetry model in the Northwestern Pacific ocean predicted from satellite altimetric vertical gravity gradient anomalies and ship-board depths," *Mar. Geodesy*, vol. 45, no. 1, pp. 24–46, Jun. 2021, doi: 10.1080/01490419.2021.1943576.
[40] R. Hao, X. Wan, and R. F. Annan, "Enhanced short-wavelength marine gravity anomaly using depth data," *IEEE Trans. Geosci. Remote Sens.*, vol. 61, 2023, Art. no. 5903109, doi: 10.1109/TGRS.2023.3242967.
[41] K. Marks and W. H. F. Smith, "Radially symmetric coherence between satellite gravity and multibeam bathymetry grids," *Mar. Geophysical Res.*, vol. 33, no. 3, pp. 223–227, Sep. 2012, doi: 10.1007/s11001-012-9157-1.
[42] X. Wan, B. Liu, X. Sui, R. F. Annan, R. Hao, and Y. Min, "Bathymetry inversion using the deflection of the vertical: A case study in South China sea," *Geodesy Geodyn.*, vol. 13, no. 5, pp. 492–502, Sep. 2022, doi: 10.1016/j.geog.2022.03.003.

Hengyang Guo is currently working toward the Ph.D. degree in surveying and mapping science and technology with the School of Land Science and Technology, China University of Geosciences, Beijing, China.

His research interest focuses on marine gravity field derivation.

Xiaoyun Wan received the Ph.D. degree in geodesy and surveying engineering from the University of Chinese Academy of Sciences, Beijing, China, in 2013.

He is currently a Professor with the School of Land Science and Technology, China University of Geosciences (Beijing), Beijing, China. His research interest focuses on space geodesy.

Huaibing Wang is currently working toward the master's degree in surveying and mapping science and technology with the School of Land Science and Technology, China University of Geosciences, Beijing, China.

His research interest focuses on seafloor bathymetry inversion.